Theoretical and Applied Mechanics Letters 15 (2025) 100615

Contents lists available at ScienceDirect

Theoretical and Applied Mechanics Letters

journal homepage: www.elsevier.com/locate/taml

Research Article

Examining eddy viscosity based LES analyses using low to moderate Reynolds number free stream turbulence due to anisotropic forcing

Hiroki Suzuki [a,*], Shinsuke Mochizuki [b], Toshinori Kouchi [a]

[a] *Graduate School of Environmental, Life Natural Science and Technology, Okayama University, 3-1-1 Tsushima-naka, Kita-ku, Okayama City 700-8530, Japan*
[b] *Graduate School of Sciences and Technology for Innovation, Yamaguchi University, 2-16-1 Tokiwadai, Ube City, 755-8611, Japan*

ARTICLE INFO

Keywords:
Turbulent flows
Anisotropic turbulence
Large-eddy simulation
Eddy viscosity
Vortical structure
Local isotropy

ABSTRACT

This study evaluates the accuracy of large-eddy simulation (LES) analyses using a commonly used subgrid-scale (SGS) model based on the eddy viscosity hypothesis. The evaluation is performed by examining the Reynolds number dependence of turbulence maintained by anisotropic and isotropic forcing techniques derived from Taylor analytical solutions. The Smagorinsky model, the Vreman model, and the coherent structure model are used as SGS models. LES outcomes were evaluated against those produced by direct numerical simulation (DNS). In contrast to the results with isotropic forcing, the turbulent kinetic energy of anisotropic forcing-induced turbulence, as calculated by DNS, exhibits a minimum in the intermediate Reynolds number range. However, all three LES analyses fail to reproduce this minimum and instead show overestimated values. This discrepancy is attributed to reduced spatial inhomogeneity of the turbulent diffusion, pressure diffusion, and pressure-strain correlation terms in the transport equations of the velocity fluctuation intensities in this Reynolds number range. Visualization results for the LES and DNS analyses further show that within this range, LES analyses reproduce two-dimensional tubular flow structures that are not observed in DNS results.

1. Introduction

Incompressible turbulence plays a critical role in improving the accuracy and efficiency of design and development processes by enabling the accurate analysis and prediction of internal flows, such as those found in flowmeters and other fluid measurement devices, as well as external flows around anemometers. Large-eddy simulation (LES) is a practical computational method for reproducing such turbulence at realistic engineering computational costs [1]. LES reduces computational costs by modeling small-scale turbulence, often based on local isotropy, while directly resolving large-scale, potentially unsteady flows through the governing equations. Although LES has a higher computational cost than Reynolds-averaged Navier-Stokes simulations [2], it offers superior fidelity in capturing flow phenomena influenced by flow unsteadiness and static pressure fluctuations. Commonly used subgrid-scale (SGS) models in LES include the Smagorinsky model [1], the Vreman model [3], and the coherent structure model [4,5]. These SGS models are constructed based on the concept of eddy viscosity and are widely implemented in various fluid simulation software [6]. In this context, the present study considers it a significant challenge to evaluate the accuracy of LES based on such SGS models.

In LES analysis, commonly used SGS models include eddy viscosity models [1] and scale similarity models [7–10]. The eddy viscosity model is considered to be the most widely used in the engineering context. Research on eddy viscosity continues to be actively conducted in recent years (e.g., [11]). The eddy viscosity coefficient used in the eddy viscosity model is isotropic, and LES analyses based on this model have been validated using isotropic turbulent fields. For isotropic turbulence, a recommended set of model constants for the Smagorinsky model has been established [12,13]. However, for non-isotropic turbulence, such as wall-bounded turbulence, different constant values may be appropriate. Wall-bounded turbulence exhibits strong anisotropy near the wall, and when using the Smagorinsky model for LES of wall-bounded turbulence, a damping function is often applied to reduce the model constant value to zero at the wall surface [1]. For LES of wall-bounded turbulence, the dynamic model is also often used [14–20]. There is a previous study reveals that minimizing the Germano-identity error along the principal strain-rate directions, rather than all components, retains the accuracy of dynamic SGS models, suggesting these directions are key to their effectiveness [21]. The dynamic model determines the zero asymptotic distribution of the model constant near the wall based on the flow field to be analyzed. Subsequently, other SGS models based on

---

* Corresponding author.
E-mail address: h.suzuki@okayama-u.ac.jp (H. Suzuki).

https://doi.org/10.1016/j.taml.2025.100615
Received 1 March 2025; Received in revised form 25 August 2025; Accepted 7 September 2025

the eddy viscosity hypothesis, such as the Vreman model and the coherent structure model, are often used [22–24]. These SGS models assume that the model constant characterizes the overall properties of the flow field. In contrast to the Smagorinsky model, these models do not require the model constant to approach zero at the wall surface. Instead, they reproduce the zero asymptotic behavior of the SGS eddy viscosity near the wall under a globally defined model constant.

In recent years, forcing methods [25,27,28] based on analytical solutions [29,30] have been used to maintain steady state turbulence. These methods introduce a forcing term into the governing equations that is proportional to the velocity field of the analytical solution with a scaling coefficient. In this context, linear forcing [31–34] uses a method that defines the forcing term based on quantities with the dimension of velocity. In the linear forcing, the forcing term is not determined by the velocity field of an analytical solution, rather by the instantaneous velocity field. When a forcing method based on Taylor's analytical solution [29,30] is used, flow structures have been reported to exist in the large-scale flow field. Furthermore, despite the steady configuration of the flow field, the turbulent energy exhibits unsteady fluctuations [25,26], which may contribute to turbulence non-equilibrium. Our research group has constructed not only anisotropic forcing fields based on Taylor's analytical solution, but also isotropic forcing fields obtained by combining these methods [27,28]. These forcing fields have been used for validation in numerical simulations in terms of conservation laws [27].

In turbulence maintained in a steady state by a forcing field based on analytical solutions, large-scale flow structures remain stationary at high Reynolds numbers. This property of stationary flow structures in such forcing fields is not observed in other forcing methods, such as the linear forcing or the random forcing. In wall-bounded turbulence, a concept of minimal flow units [35] has been used to show that flow structures can largely determine the distribution of turbulent statistics. Therefore, the stationary flow structures induced by the forcing field are expected to directly influence the fundamental turbulent statistics, such as the magnitude of the turbulent kinetic energy and the degree of anisotropy in the turbulence. On the other hand, widely used SGS models, such as the Smagorinsky model, are often based on the eddy viscosity hypothesis [1]. When applying the model, eddy viscosity is commonly assumed to be isotropic, implying that the unresolved, small-scale eddies should ideally be isotropic. Such small-scale isotropy can coexist with anisotropic large-scale turbulence only if the turbulence Reynolds number is high enough. Thus, when the turbulence Reynolds number is low to moderate and the small-scale turbulence is not isotropic, it is necessary to evaluate whether LES analysis using SGS models based on eddy viscosity can provide sufficient fidelity under such conditions.

Based on the above, the aim of this study is to evaluate the accuracy of LES analysis based on eddy viscosity SGS models for turbulence maintained by an anisotropic forcing field, which has been reported to induce stationary flow structures at high Reynolds numbers in a previous study [36], with a focus on cases at low to moderate Reynolds numbers in this study. Differences in turbulent kinetic energy, anisotropy, and coherent structures are analysed over a spectrum of Reynolds numbers, highlighting the mismatch in flow prediction between LES and DNS. The study employs an anisotropic forcing field defined by Taylor's analytical framework. This forcing field is globally anisotropic, and for comparison, the turbulence maintained by a globally isotropic forcing field constructed by combining the analytical solution is also analyzed. This study assumes that LES analysis prioritizes the characterization of large-scale turbulent statistics over that of small-scale turbulence. Consequently, the evaluation focuses on the turbulent kinetic energy as a key statistical quantity characterizing the large-scale turbulence. For the SGS models, the widely used Smagorinsky model, the Vreman model, and the coherent structure model are employed. The accuracy of LES results obtained with these models is systematically evaluated. The primary objective of this study is to systematically evaluate the fidelity of LES using eddy-viscosity-type SGS models, by comparing their predictions with DNS results under isotropic and anisotropic forcing conditions. Particular emphasis is placed on identifying discrepancies between LES and DNS in terms of turbulent kinetic energy, anisotropy, and coherent structures, and on elucidating the physical causes behind these differences.

2. Methods

The subject of the present analysis is a steady turbulent flow reproduced in a periodic cubic domain with a side length of 2π. The governing equations are the continuity equation and the Navier-Stokes equations nondimensionalized by the bulk Reynolds number Re for instantaneous velocity components u_i with x_i directions, where $i = 1, 2, 3$ and $(u, v, w) = (u_1, u_2, u_3)$. Both DNSand LES analyses are performed in this study. For the LES analysis, the filtered governing equations are used, introducing terms that include the shear stress τ_{ij}, which is the target of the SGS model application. The Navier-Stokes equations include a forcing term to stabilize the turbulence, F_i for x_i directions. This forcing term is provided based on the concept of linear forcing, $F_i = C u_i^{\mathrm{F}}$ and is configured as follows [27,28] for the anisotropic forcing field using Taylor's analytical solution [25,29,30]:

$$u_1^{\mathrm{F}} = -\cos(x_1)\sin(x_2),\ u_2^{\mathrm{F}} = \sin(x_1)\cos(x_2),\ u_3^{\mathrm{F}} = 0, \tag{1}$$

where C is a constant that determines the amplitude of the forcing field, and in this study, $C = 1$ and $C = 2$ are used. Similarly, the isotropic forcing field is constructed based on the Taylor's analytical solution shown above and is expressed as follows

$$\begin{aligned} u_1^{\mathrm{F}} &= (2/\sqrt{3})[-\cos(x_1)\sin(x_2) + \sin(x_3)\cos(x_1)], \\ u_2^{\mathrm{F}} &= (2/\sqrt{3})[-\cos(x_2)\sin(x_3) + \sin(x_1)\cos(x_2)], \\ u_3^{\mathrm{F}} &= (2/\sqrt{3})[-\cos(x_3)\sin(x_1) + \sin(x_2)\cos(x_3)], \end{aligned} \tag{2}$$

where $C = 1$ for the isotropic forcing. As shown above, both the anisotropic and isotropic forcing fields are defined as spatially distributed fields with stationary structures. In particular, when $C = 2$, the intensity of the spatial variation in the fields coincides between the two forcing types.

For the LES analysis, the Smagorinsky model [1], the Vreman model [3] and the coherent structure model [4,5] are used to model the SGS shear stress, $\tau_{ij}^{\mathrm{SGS}} = \tau_{ij} - (1/3)\delta_{ij}\tau_{kk}$ in this study. These models are based on the concept of isotropic eddy viscosity ν^{SGS} as follows

$$\tau_{ij}^{\mathrm{SGS}} = -2\nu^{\mathrm{SGS}}\,\overline{S}_{ij},\ \overline{S}_{ij} = \frac{1}{2}\left(\frac{\partial \overline{u}_i}{\partial x_j} + \frac{\partial \overline{u}_j}{\partial x_i}\right), \tag{3}$$

where $\overline{u_i}$ denotes spatially filtered velocity components for i direction. In the present analyisis, for the Smagorinsky model, the Vreman model and the coherent structure model, the SGS stress is expressed as follows:

$$\begin{aligned} \nu^{\mathrm{SGS}} &= C_{\mathrm{s}}^2\overline{\Delta}|\overline{S}_{ij}| \text{ for Smagorinsky model.} \\ \nu^{\mathrm{SGS}} &= C_{\mathrm{v}}\sqrt{B_\beta/(\alpha_{ij}\alpha_{ij})},\ \alpha_{ij} = \partial\overline{u}_j/\partial x_i,\ \beta_{ij} = \overline{\Delta}^2\alpha_{mi}\alpha_{mj},\ \text{and} \\ &\quad B_\beta = \beta_{11}\beta_{22} + \beta_{22}\beta_{33} + \beta_{33}\beta_{11} - (\beta_{12}^2 + \beta_{23}^2 + \beta_{31}^2) \\ &\quad \text{for Vreman model.} \\ \nu^{\mathrm{SGS}} &= C_{\mathrm{CS}}|F_{\mathrm{CS}}|^{3/2}\overline{\Delta}|\overline{S}_{ij}|,\ F_{\mathrm{CS}} = Q/E, \\ &\quad Q = -(1/2)(\partial\overline{u}_j/\partial x_i)(\partial\overline{u}_i/\partial x_j) \text{ and } E = (1/2)\left(\partial\overline{u}_j/\partial x_i\right)^2 \\ &\quad \text{for coherent structure model,} \end{aligned} \tag{4}$$

where $\overline{\Delta}$ denotes spatial grid width. As shown in the above equation, the coherent structure model is characterized by using the coherent structure function F_{CS} to determine the model constant of the Smagorinsky model.

Table 1
Summary of Reynolds numbers and grid resolutions used in the DNS and LES cases.

Parameters	DNS cases	LES cases
Bulk Reynolds number (Re)	10, 20, 30, 50, 100, 200, 300	
Grid resolution (N^3)	64^3 ($Re = 10$–50) 128^3 ($Re = 100$–300)	32^3 (all Re)
Subgrid-scale (SGS) models	–	Smagorinsky model, Vreman model, Coherent structure model

Table 2
Summary of subgrid-scale models and model constants used in the present study.

Parameters	LES cases with SM	LES cases with VM	LES cases with CSM
SGS models	Smagorinsky model	Vreman model	Coherent structure model
Notation of the SGS model constants	C_s	C_v	C_{CS}
Model constant values (isotropic forcing)	5.73×10^{-2}	9.38×10^{-3}	4.81×10^{-3}
Model constant values (anisotropic forcing)	1.20×10^{-1}	5.02×10^{-2}	2.54×10^{-2}

The fractional step approach is employed to integrate the governing equations. This method is based on a five-step, fourth-order Runge-Kutta scheme [37]. The Poisson equation is solved in each fractional step using a fast Fourier transform [38,39]. For the spatial discretization of the governing equations, Morinishi's conservative scheme based on the staggered grid [40] is used. Here, the spatial accuracy of all terms is fourth order. Table 1 provides a summary of the Reynolds numbers and grid resolutions. Regarding the computational conditions, the bulk Reynolds number Re is varied from $Re = 10$ to $Re = 300$. For DNS computations, the number of spatial grid points is set to $N = 64$ for $Re = 10$ to $Re = 50$ and $N = 128$ for $Re = 100$ to $Re = 300$. For the LES analysis, the number of spatial grid points is set to $N = 32$ [4]. Table 2 provides a summary of the LES models and their associated model constants. For the SGS models, it is necessary to determine the values of the model constants. In this study, the calibration values for the constants are set at $Re = 300$ so that the turbulent kinetic energy obtained from the LES analysis using each SGS model matches the corresponding value from DNS. The calibration results for the model constant of the coherent structure model are shown in Fig. 1. Here, in this study, C_s, C_v, and C_{CS} denote model constants for Smagorinsky, Vreman and coherent structure models, respeveively. As shown in the figure, for both the anisotropic and isotropic forcing fields, the turbulent kinetic energy decreases with increasing model constant values and the distribution intersects with the DNS values. Similar calibration values for the model constants are obtained for the other two SGS models. As shown in the table, The calibrated values of the model constants for the anisotropic forcing fields are $C_s = 1.20 \times 10^{-1}$, $C_v = 5.02 \times 10^{-2}$, and $C_{CS} = 2.54 \times 10^{-2}$. Similarly, for the isotropic forcing fields, $C_s = 5.73 \times 10^{-2}$, $C_v = 9.38 \times 10^{-3}$, and $C_{CS} = 4.81 \times 10^{-3}$, respectively.

3. Results and discussion

3.1. DNS-based analysis of the relationship between turbulent Reynolds number and kinetic energy

First, the isotropy of small-scale fluctuations in the generated steady turbulent field is examined. Figure 2(a) illustrates how the isotropy of small-scale fluctuations varies with the bulk Reynolds number, using the following definition:

$$I_s = \langle(\partial w/\partial z)^2\rangle / \langle(\partial u/\partial x)^2\rangle, \tag{5}$$

where $\langle\ \rangle$ denotes ensemble average for both temporal and spatial directions, and Isotropy in the small-scale eddies corresponds to $I_s = 1$. The figure confirms that, with isotropic forcing, this index stays fixed at unity for all investigated Reynolds numbers. This indicates that when the isotropic forcing field is applied, the small-scale fluctuations are isotropic, validating the isotropic forcing field used in this study. When the anisotropic forcing field is used, I_s has smaller values at low bulk Reynolds numbers. However, as the Reynolds number increases, I_s also increases, reaching and maintaining values around $I_s = 1$ for $Re \geq 100$. This result is qualitatively consistent for the two different constant values C used in the anisotropic forcing field. These results suggest that for bulk Reynolds numbers around $Re \geq 100$, local turbulence can be considered isotropic. Conversely, for smaller Reynolds numbers, it is confirmed that the anisotropy of the forcing field causes the small-scale turbulence to also exhibit anisotropy.

The forthcoming results detail the turbulent Reynolds number for the analyzed flow. The turbulent Reynolds number, based on the Taylor

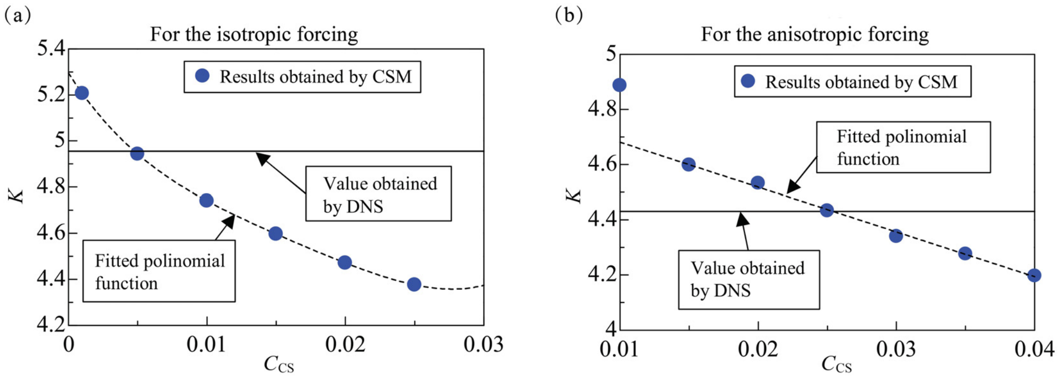

Fig. 1. Calibration of the model constant values for the coherent structure model using turbulent kinetic energy K. The K obtained in the LES analysis depending on the model constant value yields a constant value that matches that in the DNS results. (a) and (b) present the results for cases of isotropic and anisotropic forcing fields, respectively.

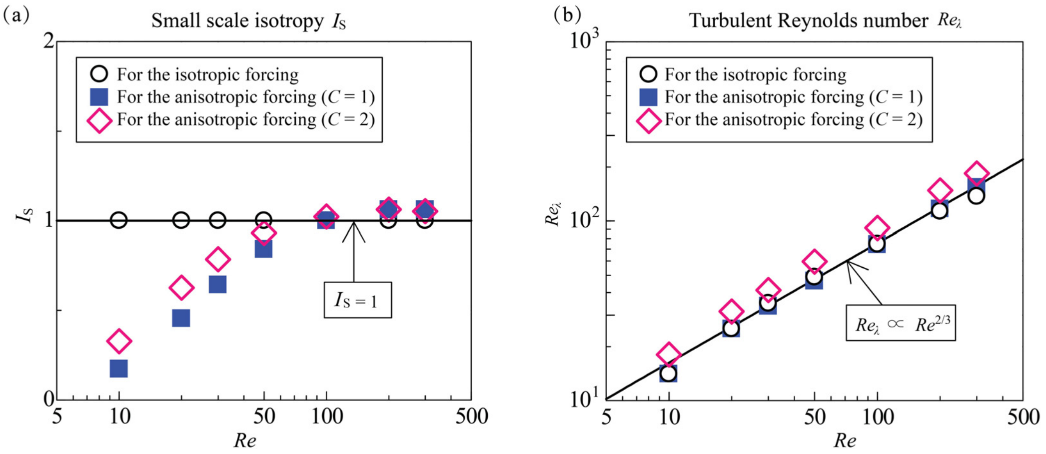

Fig. 2. (a) Reynolds number dependence of small scale isotropy I_s. (b) Reynolds number dependence of the turbulent Reynolds number Re_λ. These results are obtained in the DNS analyses and for the cases of isotropic forcing and two anisotropic forcings.

microscale, Re_λ, is defined as follows:

$$Re_\lambda = q\lambda\, Re, \text{ where } q = \sqrt{2K/3} \text{ and } \lambda = (\lambda_x\lambda_y\lambda_z)^{1/3}, \tag{6}$$

where K represents the turbulent kinetic energy; λ_x, λ_y, and λ_z denote the Taylor microscale in the x, y, and z directions, respectively. As shown in Fig. 2(b), for steady turbulence generated by isotropic forcing, the turbulent Reynolds number can be approximated as a power function of the bulk Reynolds number as follows:

$$Re_\lambda \sim Re^m, \tag{7}$$

where m is the exponent, which is determined from the figure to be $m = 2/3$. Figure 2 also includes results for turbulence generated by anisotropic forcing. As shown, the distribution of turbulent Reynolds numbers for $C = 2$ does not coincide with the distribution for isotropic forcing, while the distribution for $C = 1$ is observed to coincide with the distribution for isotropic forcing. This finding indicates that setting the anisotropic forcing coefficient C to $C = 1$ ensures that the turbulent Reynolds numbers generated by anisotropic and isotropic forcing fields are consistent. Therefore, in this study, subsequent analyses of anisotropic forcing will use the results obtained with $C = 1$.

Figure 3 presents the relationship between the bulk Reynolds number and the turbulent kinetic energy K. Here, the turbulent kinetic energy is a statistical quantity obtained as the spatially averaged value over the entire computational domain, as follows $K = (1/2)(\langle u^2\rangle + \langle v^2\rangle + \langle w^2\rangle)$. In the case of isotropic forcing, as shown in the figure, the turbulent kinetic energy increases with the bulk Reynolds number. In this analysis, the magnitude of the forcing is predefined, and the spatial length scale of the large-scale flow is also determined by the forcing field. Meanwhile, the dissipation coefficient is observed to decrease with increasing Reynolds number in the low turbulence Reynolds number range. These factors are considered to contribute to the monotonic increase in the mean turbulent kinetic energy with the Reynolds number observed in this study. Figure 3 also includes the turbulent kinetic energy of turbulence maintained by an anisotropic forcing field with $C = 1$. As shown, unlike the case of isotropic forcing, the turbulent kinetic energy of turbulence under anisotropic forcing exhibits a minimum at intermediate Reynolds numbers. For Reynolds numbers higher than this minimum, the turbulent kinetic energy of turbulence driven by anisotropic forcing increases with increasing Reynolds number.

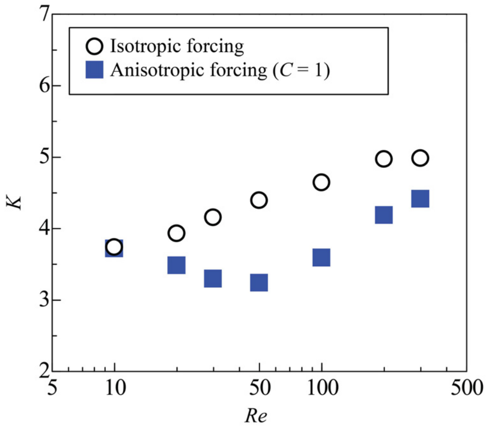

Fig. 3. Reynolds number dependence of turbulent kinetic energy K obtained by DNS analysis. The distributions presented are for isotropic and anisotropic forcing fields with $C = 1$.

3.2. *Evaluation of large-scale anisotropy using the Lumley triangle representation*

Figure 4 (a) illustrates the variation of large-scale isotropy with the bulk Reynolds number, defined as follows:

$$I_L = \langle w^2\rangle / \langle u^2\rangle, \tag{8}$$

where $I_L = 1$ corresponds to the case where the turbulence is isotropic. When an anisotropic forcing field is applied, the nature of the field ensures that $\langle v^2\rangle = \langle u^2\rangle$. As shown in the figure, in the case of turbulence maintained by isotropic forcing, the large-scale isotropy remains at I_L =1 regardless of the bulk Reynolds number. This result validates the turbulence generated by the isotropic forcing field used in this study. The figure also shows the large-scale isotropy results for turbulence driven by an anisotropic forcing field. As shown, in this case the isotropy I_L increases with Reynolds number at lower bulk Reynolds numbers. For $Re \geq 100$, the I_L becomes approximately constant, independent of further increases in Reynolds number. The minimum Reynolds number at which the I_L reaches constant isotropy corresponds to the minimum Re at which the small-scale turbulence becomes isotropic, as shown in the figure.

To investigate the degree of anisotropy in large-scale turbulence, the anisotropy tensor [1] is used. The anisotropy tensor b_{ij} is given as follows:

$$b_{ij} = \langle u_i u_j\rangle / \langle u_k u_k\rangle - (1/3)\delta_{ij}, \tag{9}$$

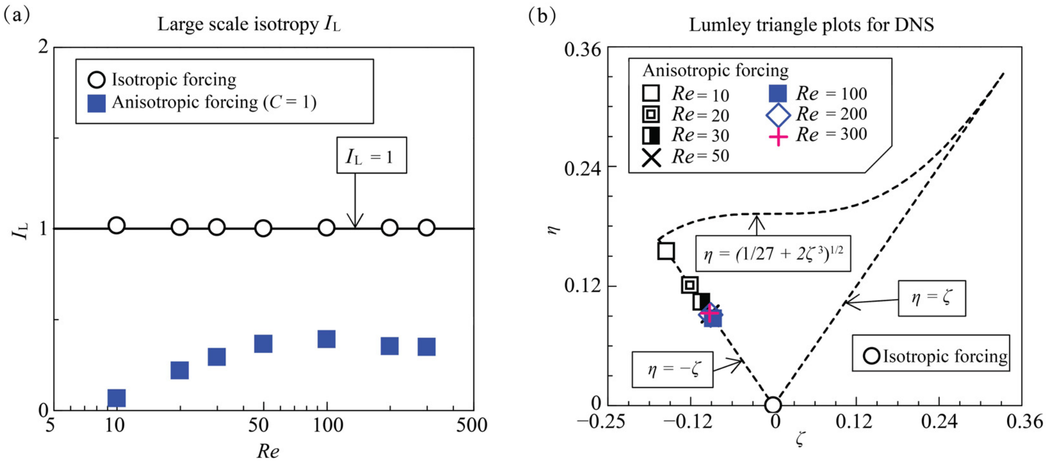

Fig. 4. (a) Reynolds number dependence of large scale isotropic I_{L}. (b) Reynolds number dependence of large scale isotropy expressed using Lumley triangles. Here, these results are obtained by DNS analysis.

where $i = 1 - -3$, $j = 1 - -3$, and the summation is taken over k. Using the parameters η and ξ, defined as follows:

$$6\eta^2 = b_{kk}^2 \text{ and } 6\xi^3 = b_{kk}^3. \qquad (10)$$

The characteristics of the turbulence anisotropy can be classified using the above parameters. Specifically: if $\eta = \xi = 0$, the turbulence is isotropic. When $\xi = -1/6$ and $\eta = 1/6$, the turbulence is two-component anisotropic. If $\xi = 1/3$ and $\eta = 1/3$, the turbulence is one-component anisotropic. When $\eta = \xi$, the turbulence has axisymmetric anisotropy with a large eigenvalue. When $\eta = -\xi$, the turbulence has axisymmetric anisotropy with a small eigenvalue. When $\eta = \sqrt{1/27 + 2\xi^3}$, the turbulence has two-component anisotropy. These relationships are organized using the Lumley triangle [1] shown in Fig. 4(b). In the figure, the triangle is represented by dashed lines. The turbulence values generated by isotropic and anisotropic forcing fields are plotted on this triangle. As shown in the figure, in the case of turbulence generated by isotropic forcing, the plots consistently lie at $\eta = \xi = 0$, regardless of the bulk Reynolds number. This again confirms that the turbulence generated by isotropic forcing is isotropic. Figure 4(b) similarly presents the Reynolds-number trend for turbulence produced under anisotropic forcing. As shown, the plots lie along the line $\eta = -\xi$ regardless of the Reynolds number. This indicates that the anisotropic turbulence has an axisymmetric anisotropy with a small eigenvalue. As shown in the figure, for $Re = 10$, the plot is closest to the point $\xi = -1/6$ and $\eta = 1/6$. As the Reynolds number increases, the plots move further away from this point and approach a convergence point. This behavior corresponds to the earlier results for large-scale turbulence isotropy, where $I_{\mathrm{L}} = \langle w^2 \rangle / \langle u^2 \rangle$ increases with the Reynolds number and eventually converges to a certain value.

Figure 5 presents a comparison of the plots of turbulence generated by anisotropic forcing obtained from LES with those from DNS using the Lumley triangle. In addition to the results from the three SGS models, the results from implicit LES are also included. As demonstrated in the figure, the result observed in DNS, where the plots lie along the line $\eta = -\xi$, is similarly observed in all LES results. For the range of Reynolds numbers from $Re = 10$ to 50, the LES plots generally align with the DNS results. This range corresponds to the region where local turbulence is not isotropic, as indicated in the earlier figure showing the anisotropy of small-scale turbulence. Conversely, for Reynolds numbers ranging from 100 to 300, the LES plots appear to deviate from those of DNS. This discrepancy is observed not only in the results from the three LESs using SGS models but also in the results from implicit LES without SGS models. As indicated in the preceding figure, the range of Reynolds numbers exhibiting this discrepancy matches the interval in which the small-scale motions are effectively isotropic.

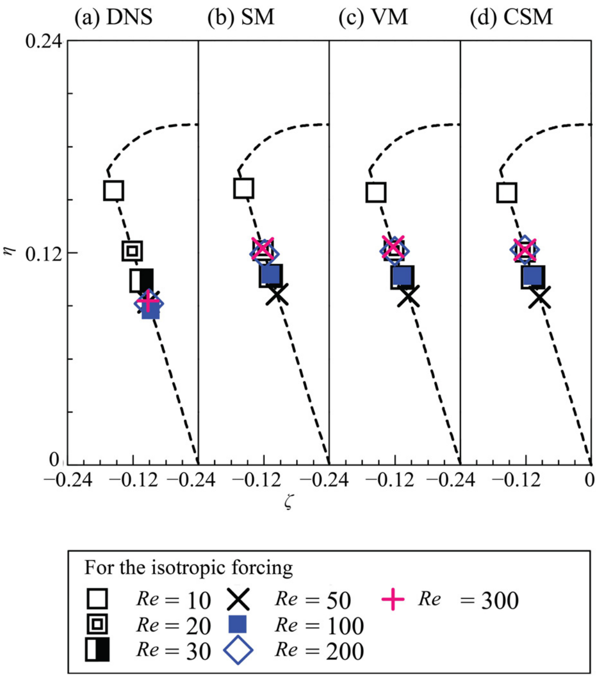

Fig. 5. Reynolds number dependence of the large-scale isotropy obtained in the LES analysis compared to the DNS results shown in (a) using Lumley triangle. Here, (b), (c) and (d) show the results for the Smagorinsky model, the Vreman model and the coherent structure model, respectively.

3.3. *Discrepancy in turbulent kinetic energy between LES and DNS at intermediate Reynolds numbers*

Figure 6 compares the Reynolds number dependence of turbulent kinetic energy obtained using LES with that obtained from DNS. The results are presented for both anisotropic and isotropic forcing cases. The DNS results presented in the figure are a reproduction of those shown earlier. For turbulence generated by anisotropic forcing, as shown in Fig. 6(a), the LES results generally align with the DNS results within the range of $Re = 10$ to $Re = 40$. This observation is consistently observed

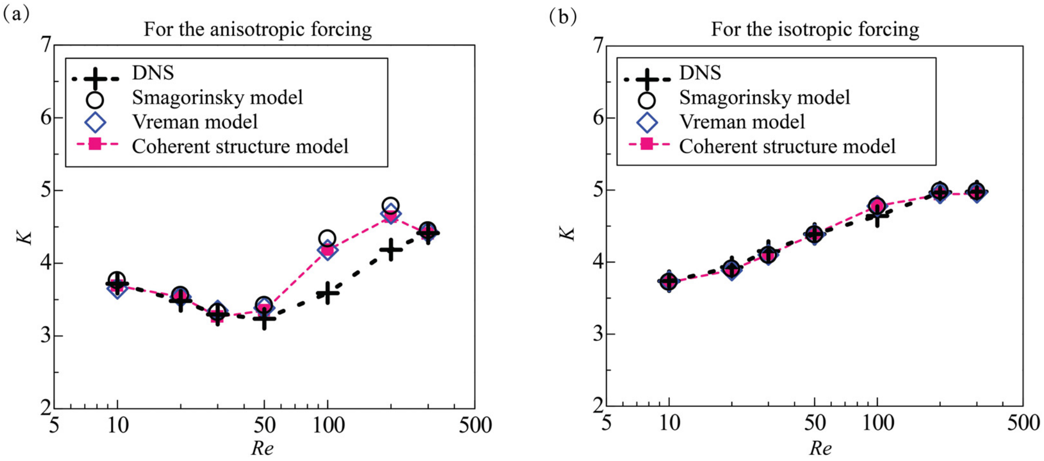

Fig. 6. Reynolds number dependence of turbulent kinetic energy obtained by the LES analyses based on the three SGS models compared to that of the DNS. The results for the anisotropic and isotropic forcing fields are shown in (a) and (b), respectively.

across all three SGS models. However, within the range of $Re = 50$ to $Re = 200$, the LES results deviate from the DNS results, exhibiting higher values. The Vreman model and coherent structure model, despite their capacity to automatically reduce SGS eddy viscosity to zero in laminar regions such as near wall surfaces, also fail to match the DNS results. Their output is generally consistent with the plots from the Smagorinsky model. Figure 6(b) compares LES results with DNS results for turbulence generated by isotropic forcing. As shown in the figure, in the case of isotropic forcing, the LES results demonstrate a high degree of agreement with the DNS results across all Reynolds numbers. This agreement is consistently observed across all three SGS models. In sharp contrast to the findings for isotropic forcing, discrepancies are observed in the LES results for anisotropic forcing.

3.4. Enhanced spatial homogeneity at intermediate Reynolds numbers indicated by the transport equation of velocity fluctuation intensities

Focusing on turbulence produced under anisotropic forcing, the study assesses Reynolds-number effects on turbulent kinetic energy through the transport equation for relevant statistical quantities [1]. Specifically, the balance of the transport equation for velocity fluctuation intensities, derived from the decomposition of turbulent kinetic energy, is calculated. The transport equations for velocity fluctuation $\langle u_i^2\rangle_t$ intensities corresponds to the case where $i = j$ in the transport equations for Reynolds stress $\langle u_iu_j\rangle_t$, where $\langle\ \rangle_t$ denotes time-averaging operation. The transport equations for Reynolds stress $\langle u_iu_j\rangle_t$ is expressed as follows:

$$\begin{aligned}\frac{\partial\langle u_iu_j\rangle_t}{\partial t} &= A_{ij} + P_{ij} - \epsilon_{ij} + \Pi_{ij} + D^T_{ij} + D^p_{ij} + D^v_{ij} + f_{ij},\ \text{where}\\ A_{ij} &= -\partial(\langle u_iu_j\rangle_t U_k)/\partial x_k,\ P_{ij} = -\langle u_iu_k\rangle_t(\partial U_j/\partial x_k) - \langle u_ju_k\rangle_t(\partial U_i/\partial x_k),\\ \epsilon_{ij} &= \frac{2}{Re}\langle(\partial u_i/\partial x_k)(\partial u_j/\partial x_k)\rangle_t,\ \Pi_{ij} = \langle p(\partial u_i/\partial x_j + \partial u_j/\partial x_i)\rangle_t,\\ D^T_{ij} &= -\partial\langle u_iu_ju_k\rangle_t/\partial x_k,\ D^p_{ij} = -\partial(\langle pu_i\rangle_t\delta_{jk} + \langle pu_j\rangle_t\delta_{ik}),\\ D^v_{ij} &= \partial((1/Re)\partial\langle u_iu_j\rangle_t/\partial x_k),\ \text{and}\ f_{ij} = \langle u_iF_j\rangle_t + \langle u_jF_i\rangle_t,\end{aligned} \tag{11}$$

where U_i is temporal mean velocity for i direction. The transport equation consists of the following terms: the convection term, the production term, the viscous dissipation term, the pressure-strain correlation term, the turbulent diffusion term, the pressure diffusion term, the viscous diffusion term, and a contribution term from forcing. It is expected that energy is injected into the system per unit time via the contribution term from forcing, considering the entire computational domain. The viscous dissipation term quantifies the dissipation of velocity fluctuation intensities as an energy quantity due to viscosity, while the pressure-strain correlation term redistributes energy among the components of velocity fluctuation intensities. The three diffusion terms mitigate spatial inhomogeneities in the distribution of velocity fluctuation intensities. In this study, the analysis of the transport equation for Reynolds stress components is conducted exclusively using DNS results. This decision is based on the fundamental difference between DNS and LES formulations. In LES, spatial filtering introduces additional SGS stress terms that are modeled by eddy-viscosity-based assumptions, resulting in governing equations that are structurally and physically distinct from those of DNS. Due to these differences, the transport equation terms in LES, such as SGS dissipation and modeled pressure-strain effects, cannot be directly compared with their DNS counterparts. A term-wise comparison between DNS and LES would therefore be inconsistent and potentially misleading. To ensure physical interpretability without the influence of SGS model dependencies, the present analysis focuses solely on DNS-based equations.

As demonstrated in Fig. 7, the balance of velocity fluctuation intensities is contingent upon the Reynolds number. In the context of turbulence driven by anisotropic forcing, the results for both intensities of the velocity fluctuations denoted as $\langle u^2\rangle$ and $\langle w^2\rangle$ are presented. Here, the magnitude of each term shown is the spatially averaged value. As demonstrated in Fig. 7(a), for turbulence driven by anisotropic forcing, the energy introduced via the forcing term is balanced by the sum of the redistribution of energy to the $\langle w^2\rangle$ component through the pressure-strain correlation terms and viscous dissipation. The magnitudes of the other terms are spatially averaged to zero over the entire domain. The energy budget for velocity-fluctuation intensities shows that contributions from the pressure-strain correlation terms to the componentwise kinetic energy are exactly counteracted by viscous dissipation. In contrast, as shown in Fig. 7(b), for turbulence driven by isotropic forcing, the energy input via the forcing term balances only with viscous dissipation. The spatially averaged values of each term remain approximately constant with respect to Reynolds number, except for the low Reynolds number condition. This result, where the spatially averaged values of each term exhibit no significant Reynolds number dependence, can also be observed in the case of turbulence driven by anisotropic forcing. However, it differs in distribution shape from the Reynolds number dependence of turbulent kinetic energy for anisotropic forcing, which exhibits a minimum value, as shown in the earlier figure. This discrepancy suggests that the spatially averaged balance of velocity fluctuation intensities may not adequately explain the turbulent kinetic energy

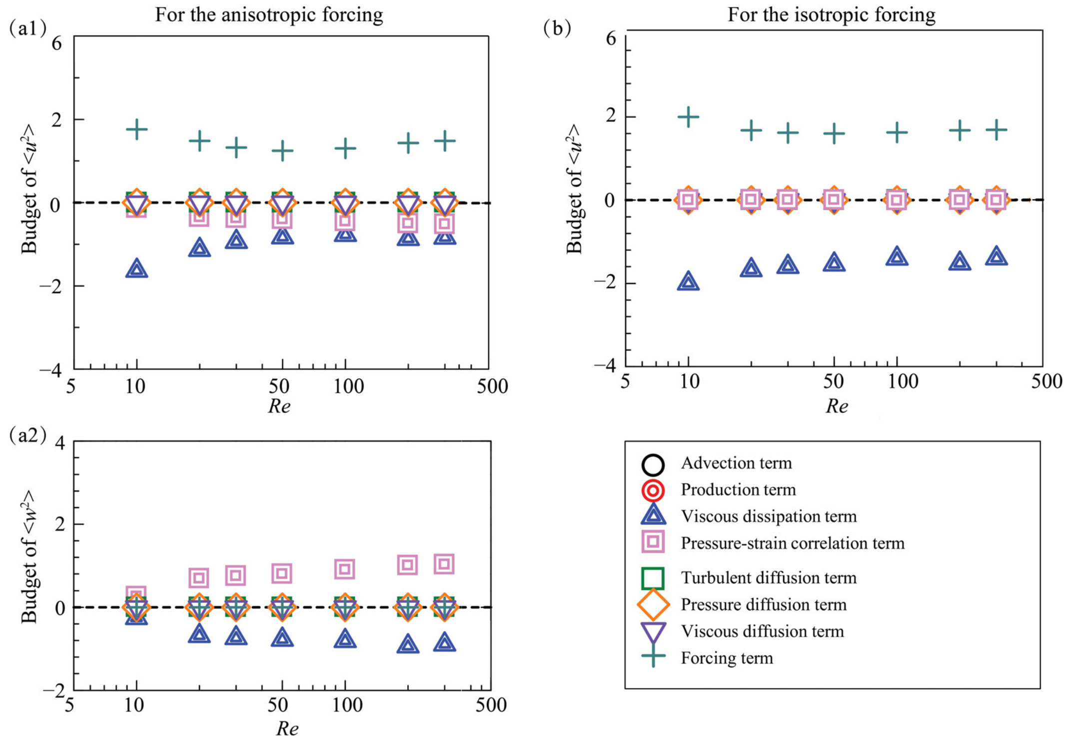

Fig. 7. Mean values of each term in the transport equation for the velocity fluctuation intensities, shown as the Reynolds number dependence. Here, (a1) and (a2) present the results for $\langle u^2 \rangle$ and $\langle w^2 \rangle$ of turbulence due to the anisotropic forcing field, while (b) presents the results for $\langle u^2 \rangle$ in the case of the isotropic forcing.

distribution with a minimum value observed in the case of anisotropic forcing.

The present study focuses on the spatial inhomogeneity of the terms in the transport equations, in light of the preceding results. Given the spatial variations of the forcing field defined in this study, the statistical distributions of the turbulence stabilized by this field may be spatially inhomogeneous. As shown in Fig. 8(a), the root-mean-square (RMS) deviations of the terms in the transport equation from their spatially averaged values are presented for turbulence generated by the anisotropic forcing. As the figure illustrates, the turbulent diffusion terms, pressure diffusion terms, and pressure-strain correlation terms demonstrate higher spatial inhomogeneity compared to other terms. Furthermore, this inhomogeneity is observed to depend on the bulk Reynolds number, with the spatial inhomogeneity of these three terms reaching a minimum around $Re = 50$. This observation is consistent with the findings in Fig. 6(a), which depicts the bulk Reynolds number dependence of turbulent kinetic energy for turbulence generated by anisotropic forcing, also exhibiting a minimum around $Re = 50$. The distribution shapes of the spatial inhomogeneity of these three terms, as indicated by this result, qualitatively resemble the distribution of turbulent kinetic energy. Figure 8(b) presents the RMS deviations of the terms in the transport equation for turbulence generated by isotropic forcing as a function of

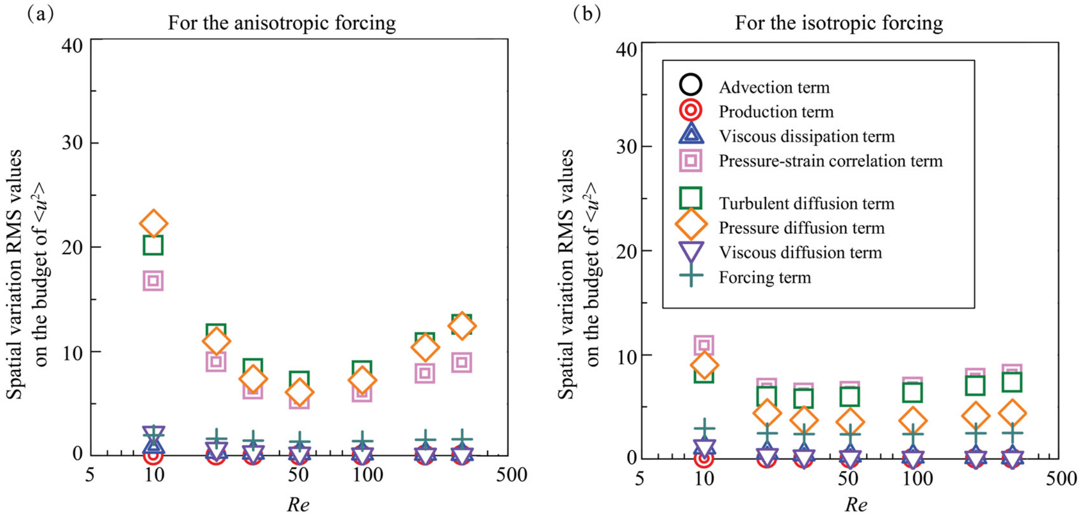

Fig. 8. Spatial variation RMS values for each term of the transport equation for the velocity fluctuation intensity $\langle u^2 \rangle$, shown as a Reynolds number dependence. (a) and (b) present the results for the turbulent version with the anisotropic and isotropic forcing fields.

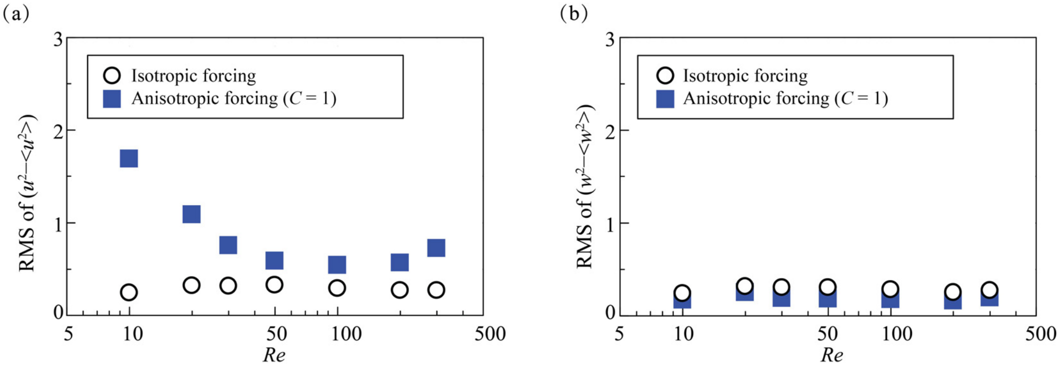

Fig. 9. Reynolds number dependence of the RMS of the spatial variation of the velocity fluctuation intensity. Here, (a) and (b) represent the results for RMS values of $(u^2 - \langle u^2 \rangle)$ and $(w^2 - \langle w^2 \rangle)$.

Re. As demonstrated in the figure, even for turbulence generated by isotropic forcing, the RMS deviations of the turbulent diffusion term, pressure diffusion term, and pressure-strain correlation term are larger than those of the other terms. However, the Reynolds number dependence of the RMS deviations for these three terms is smaller in the case of isotropic forcing than in the case of anisotropic forcing.

Figure 9 illustrates the spatial RMS deviation of velocity fluctuation intensities, $\langle u^2 \rangle$ and $\langle w^2 \rangle$, from their spatial averages as a function of the bulk Reynolds number. In the context of spatially homogeneous velocity fluctuation intensities, the spatial RMS deviation is equivalent to zero. As demonstrated in Fig. 9, for turbulence driven by the anisotropic forcing, the spatial RMS deviation of $\langle u^2 \rangle$ varies with the Reynolds number. This deviation attains a minimum around $Re = 100$. At lower Reynolds numbers, the RMS deviation decreases with increasing Re, approaching this minimum. At higher Reynolds numbers, the RMS deviation increases as Re rises beyond the minimum. The anisotropic forcing field applied in this study remains constant across all Reynolds numbers. Consequently, this result suggests that the spatial homogenity of the generated turbulence changes, reaching its highest level around $Re = 100$. However, this Reynolds number dependence of the RMS deviation is not observed for the second intensity $\langle w^2 \rangle$. In contrast, for turbulence driven by isotropic forcing, the spatial RMS deviation remains approximately constant across all Reynolds numbers and is smaller than that observed in the case of anisotropic forcing. This indicates that the spatial uniformity of turbulence statistics under isotropic forcing remains nearly constant with respect to the Reynolds number and is higher than that under the anisotropic forcing.

3.5. Flow structure analysis reflecting the increased spatial uniformity in the intermediate Reynolds number regime

Figure 10 now offers a four-way comparison of flow visualizations obtained from DNS and the three eddy-viscosity SGS models (Smagorinsky, Vreman, and the coherent-structure model). All frames display green isosurfaces of negative static-pressure fluctuation because this quantity remains robust even on the coarser LES grids and therefore provides a scale-consistent indicator of the large-scale tube-like vortices generated by the anisotropic forcing. Although the Q-criterion (the second invariant of the velocity-gradient tensor) is also plotted as white isosurfaces in the DNS panels, it is intentionally omitted from the LES panels: the enhanced numerical and subgrid dissipation in LES, combined with the larger grid spacing, suppresses the small-scale vortical signal and yields sparsely distributed Q isosurfaces that obscure, rather than clarify, the intended large-scale comparison. This unified visualization therefore isolates the capability of each SGS model to reproduce (or over-predict) the deterministic two-dimensional tubular structures while avoiding artefacts introduced by under-resolved Q-criterion fields. For the DNS cases shown in Fig. 10(a1)–(c1), the white surfaces signify the isosurfaces of the second invariant of the velocity gradient tensor, thus emphasizing small-scale turbulence structures. The results are presented for $Re = 10,\ 100,\ 300$ based on the Reynolds-number-dependent distribution of turbulent kinetic energy. As demonstrated in the figures, for the DNS results at both $Re = 10$ and $Re = 300$, two-dimensional tubular flow structures, rendered by the green isosurfaces, are discernible. Conversely, at $Re = 100$, such tubular structures are not observed, and appear more fragmented. The stable presence of tubular flow structures is considered to enhance the spatial inhomogeneity of the turbulence, while the absence of such structures at a Reynolds number of 100 is thought to reduce the spatial inhomogeneity of the turbulence. This observation is qualitatively consistent with the earlier findings of the three terms in the transport equation and the low spatial inhomogeneity of velocity fluctuations observed at a Reynolds number between 50 and 100. Figure 10(a2)–(c2), (a3)–(c3), and (a4)–(c4) illustrate the visualization outcomes of anisotropic turbulence, as predicted by the Smagorinsky model, vreman model, and the coherent structure model, respectively, as functions of the Reynolds number. As demonstrated, for specific values of the Reynolds number, namely, 10 and 300, the flow fields obtained from both LES analyses exhibit two-dimensional tubular structures that are analogous to those observed in the DNS results.

Conversely, at $Re = 100$, such tubular structures are not clearly observed and appear more fragmented. This result was confirmed to be robust across a range of negative pressure thresholds used for the visualization, as well as at multiple time instances under statistically steady conditions. It should be noted that the formation of the tubular structures is induced by the anisotropic spatial structure of the forcing field, and their appearance at high Reynolds numbers is a consequence of the periodicity and symmetry embedded in the forcing—thus, such structures are expected to emerge deterministically. However, at $Re = 100$, the breakdown of these tubular structures was found to occur intermittently over time, suggesting that their absence is not static but rather temporally varying. This behavior is clearly illustrated in Fig. 11, where large-scale vortex structures characterized by negative static pressure fluctuations are visualized at several time instances. According to the figure, well-defined tubular formations are less apparent in the DNS results for $Re = 100$ than for the higher Reynolds numbers. and the overall flow field is dominated by fragmented and unstable patterns. Nevertheless, temporal observations confirm that the disappearance of these structures occurs in an intermittent and transient manner. In other words, the dynamics at $Re = 100$ suggest the existence of periodic or quasi-periodic collapse and reconstruction of the tubular structures. Such breakdown phenomena are not prominently observed in the LES results, where two-dimensional vortex tubes are stably sustained at many time instances. The mechanism of this intermittent disappearance and reappearance of the tubular structures remains an open issue and is expected to be addressed in future studies through time-resolved statistical and spectral analyses.

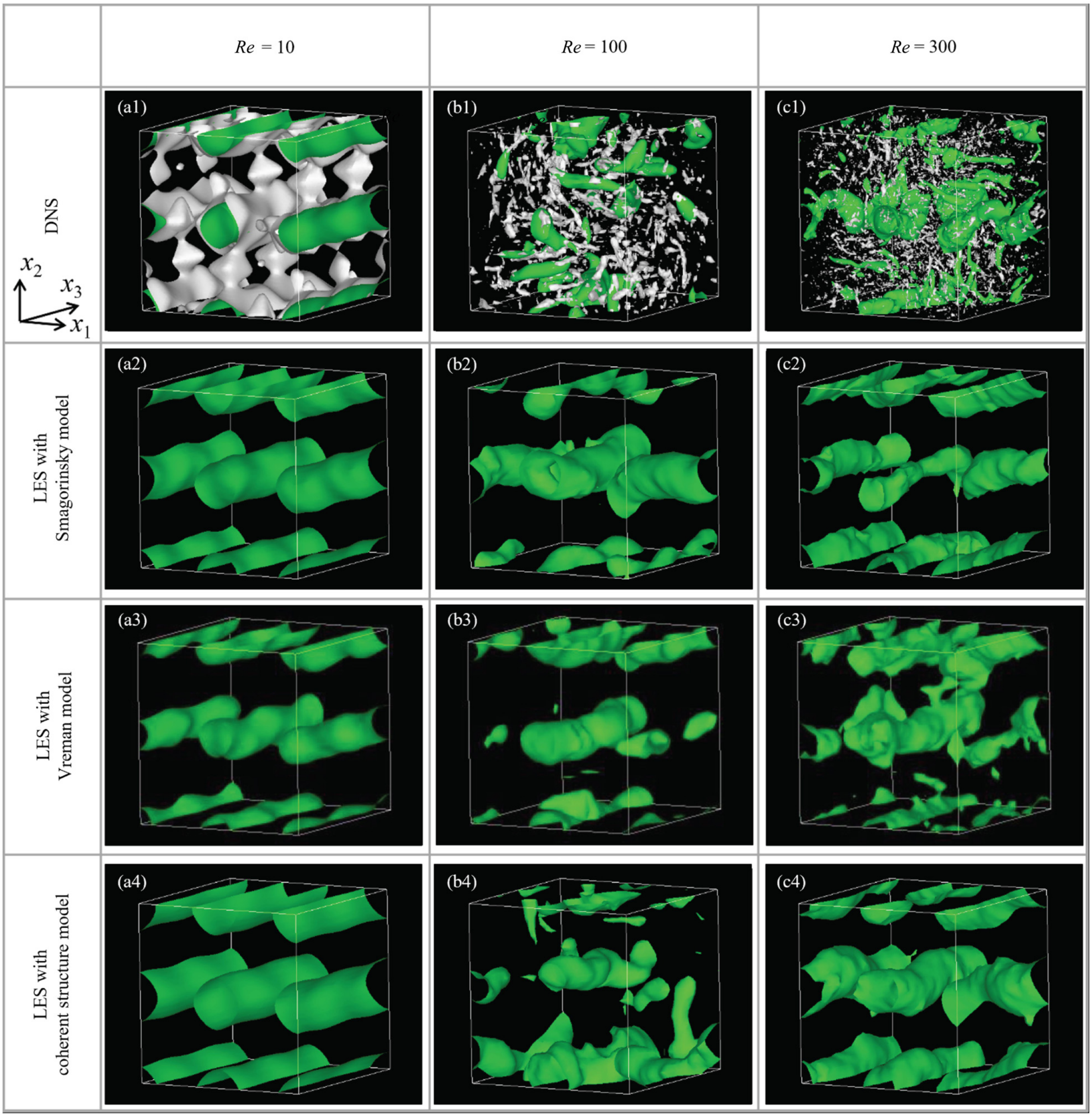

Fig. 10. Visualization of turbulence structures under anisotropic forcing at $Re = 10,\ 100,\ 300$ using DNS and LES with three SGS models: Smagorinsky, Vreman, and the Coherent Structure Model (CSM). Green isosurfaces represent regions of negative static pressure fluctuation, highlighting large-scale coherent structures. The coordinate system (x_1, x_2, x_3) is also shown in the visualization, where x_1 and x_2 define the plane in which the anisotropic forcing field, shown in Eq. (1), actively induces organized two-dimensional tubular structures. The visualization thus reflects the expected periodic structures aligned along the x_1-x_2 plane. In the DNS results (top row), white isosurfaces show positive values of the Q-criterion, visualizing small-scale vortex cores. For LES cases (rows-4), only pressure-based isosurfaces are shown, as Q-criterion is less meaningful due to coarse resolution and strong subgrid-scale dissipation. The comparison clarifies how coherent structures are represented across models and Reynolds numbers.

This finding is in qualitative disagreement with the DNS visualization results. The Reynolds-number-dependent distribution of turbulent energy obtained from DNS demonstrates that the increase in turbulence inhomogeneity corresponds qualitatively to the increase in turbulent energy. These visualization results suggest that the LES analyses reproduce two-dimensional tubular structures that are not observed in the DNS results, indicating that the inhomogeneity of turbulence is enhanced, thereby increasing turbulent kinetic energy. At $Re = 100$, the turbulent kinetic energy in LES was significantly overestimated compared to DNS, particularly with the Smagorinsky model. This discrepancy is attributed to the inability of the eddy-viscosity SGS models to capture the transient collapse of coherent structures observed in the DNS. While LES predicts persistent two-dimensional tubular structures, DNS results show intermittent fragmentation, which leads to lower spatial inhomogeneity and reduced energy. These differences in structure and transport terms provide a physical basis for the divergence in flow predictions between LES and DNS.

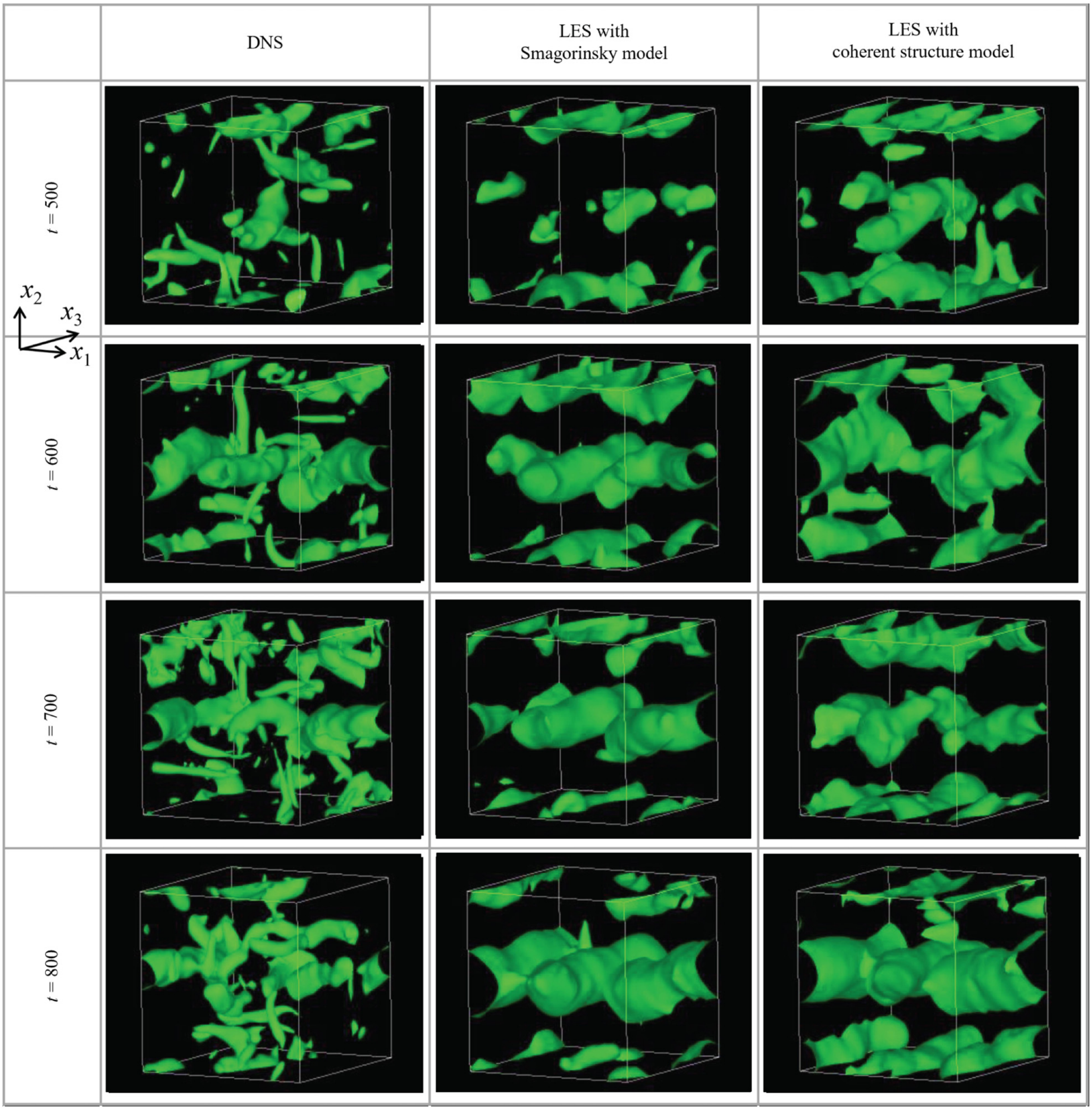

Fig. 11. Comparison between DNS and LES of large-scale structures visualized using negative static pressure fluctuations at $Re = 100$. The results include those obtained using the Smagorinsky model and a coherent structure model that shares a similar formulation for the eddy viscosity term. As shown in the figure, the DNS results frequently exhibit an absence of pronounced two-dimensional vortex tube structures, and no dominant vortex patterns are observed at many instances. In contrast, the LES field often displays two-dimensional vortex tubes at various moments. However, it should be noted that even in LES, there are instances where such vortex tubes are not observed.

4. Conclusion

The aim of this study is to examine the fidelity of LES analyses employing SGS viscosity models, with a particular emphasis on the low to moderate Reynolds number range. The study utilizes three widely adopted SGS models: the Smagorinsky model, the Vreman model, and the coherent structure model. The Taylor analytical solution is employed to establish the anisotropic forcing field, which stabilizes turbulence. The isotropic forcing field constructed from the same analytical solution is utilized for comparative analysis. The generation of turbulence occurs within a periodic cubic domain with a side length of 2π. The governing equations are solved using the fractional-step method based on a fifth-stage, fourth-order Runge-Kutta scheme. The fourth-order central difference method, developed by Morinishi et al., is employed for evaluating spatial differentiation.The bulk Reynolds number, Re, is varied from 10 to 300. At the maximum value of Re, the small-scale turbulence is considered isotropic. Under this condition, the model constants of each SGS model are calibrated using the DNS results.

This study clarified the fidelity and limitations of LES predictions by systematically comparing them with DNS results under isotropic and anisotropic forcing. Through quantitative comparisons of turbulent kinetic energy, anisotropy tensors (via the Lumley triangle), and flow structure visualizations, the analysis highlighted how eddy-viscosity-type SGS models affect the accuracy of LES under moderate Reynolds numbers. The discrepancies observed, particularly in the intermediate Reynolds number regime, were further interpreted based on transport equation terms and spatial inhomogeneity metrics. The anisotropy of these two types of turbulence was investigated using large-scale anisotropy and the Lumley triangle. The accuracy of reproducing DNS results through LES analysis was evaluated using the Lumley triangle. Subsequently, the Reynolds number dependency of turbulent energy revealed that, in the case of turbulence driven by anisotropic forcing, the turbulent energy obtained from LES was larger than that from DNS in the intermediate Reynolds number range. This discrepancy was not observed in the case of turbulence generated by isotropic forcing. These results qualitatively align with the Reynolds number dependency of the transport equation for velocity fluctuation intensity and the spatial inhomogeneity of velocity fluctuations. Furthermore, the Reynolds number dependency of flow structures in turbulence generated by anisotropic forcing was visualized and compared between DNS and LES results. At a Reynolds number of 100, where the discrepancy in turbulent energy was observed, the DNS results exhibited no two-dimensional tubular structures, whereas the LES results reproduced such structures. This disparity in the reproduction of flow structures suggests that it characterizes the discrepancy between LES and DNS results. The present results demonstrate that LES using eddy-viscosity SGS models exhibits notable discrepancies from DNS, especially at $Re = 100$. These discrepancies arise from limitations in reproducing the anisotropic redistribution and temporal intermittency of coherent structures. Further refinement of SGS models or non-isotropic closure approaches may be required to improve LES fidelity in this regime.

Declaration of competing interest

The authors declare the following financial interests/personal relationships which may be considered as potential competing interests: Hiroki Suzuki reports financial support was provided by JSPS KAKENHI. If there are other authors, they declare that they have no known competing financial interests or personal relationships that could have appeared to influence the work reported in this paper.

CRediT authorship contribution statement

Hiroki Suzuki: Funding acquisition, Writing – review & editing, Writing – original draft, Visualization, Validation, Methodology, Investigation, Formal analysis, Data curation, Conceptualization. **Shinsuke Mochizuki:** Writing – review & editing, Supervision, Funding acquisition, Conceptualization. **Toshinori Kouchi:** Writing – review & editing, Funding acquisition, Conceptualization, Methodology.

Acknowledgments

The authors are deeply grateful to Mr. Shotaro Jomura (Yamaguchi University) and Ms. Mayuka Oshibuchi for their assistance in carrying out this work, and to Prof. Christopher Keylock (Loughborough University) for his insights into this work. This work was supported by the Japanese Ministry of Education, Culture, Sports, Science and Technology through Grants-in-Aid (Grant Nos. 21K03859 and 22H01684), the Kurita Water and Environment Foundation (Grant No. 25B042), and the Okayama Foundation for Science and Technology (2025).

References

[1] S.B. Pope, Turbulent Flows, Cambridge University Press, 2001.
[2] H. Xiao, P. Cinnella, Quantification of model uncertainty in RANS simulations: a review, Prog. Aerosp. Sci. 108 (2019) 1–31.
[3] A.W. Vreman, An eddy-viscosity subgrid-scale model for turbulent shear flow: algebraic theory and applications, Phys. Fluids 16 (2004) 3670–3681.
[4] H. Kobayashi, The subgrid-scale models based on coherent structures for rotating homogeneous turbulence and turbulent channel flow, Phys. Fluids 17 (2005) 045104.
[5] H. Kobayashi, F. Ham, X. Wu, Application of a local SGS model based on coherent structures to complex geometries, Int. J. Heat Fluid Flow 29 (2008) 640–653.
[6] E. Komen, A. Shams, L. Camilo, B. Koren, Quasi-DNS capabilities of openFOAM for different mesh types, Comput. Fluids 96 (2014) 87–104.
[7] C. Meneveau, J. Katz, Scale-invariance and turbulence models for large-eddy simulation, Annu. Rev. Fluid Mech. 32 (2000) 1–32.
[8] K.I. Abe, An improved anisotropy-resolving subgrid-scale model with the aid of a scale-similarity modeling concept, Int. J. Heat Fluid Flow 39 (2013) 42–52.
[9] H. Kobayashi, Improvement of the SGS model by using a scale-similarity model based on the analysis of SGS force and SGS energy transfer, Int. J. Heat Fluid Flow 72 (2018) 329–336.
[10] R. Agrawal, M.P. Whitmore, K.P. Griffin, S.T. Bose, P. Moin, Non-boussinesq subgrid-scale model with dynamic tensorial coefficients, Phys. Rev. Fluids 7 (2022) 074602.
[11] J.A. Domaradzki, Autonomous large-eddy simulations of turbulence using eddy viscosity derived from the subgrid-scale similarity stress tensor, J. Fluid Mech. 985 (2024) A48.
[12] V.M. Canuto, Y. Cheng, Determination of the Smagorinsky-Lilly constant CS, Phys. Fluids 9 (5) (1997) 1368–1378.
[13] N. Park, S. Lee, J. Lee, H. Choi, A dynamic subgrid-scale eddy viscosity model with a global model coefficient, Phys. Fluids 18 (2006) 125109.
[14] M. Germano, U. Piomelli, P. Moin, W.H. Cabot, A dynamic subgrid–scale eddy viscosity model, Phys. Fluids A 3 (1991) 1760–1765.
[15] D.K. Lilly, A proposed modification of the Germano sugrid-scale closure method, Phys. Fluids A 4 (1992) 633–635.
[16] A. Yoshizawa, M. Tsubokura, T. Kobayashi, N. Taniguchi, Modeling of the dynamic subgrid–scale viscosity in large eddy simulation, Phys. Fluids 8 (1996) 2254–2256.
[17] Y. Morinishi, O.V. Vasilyev, Vector level identity for dynamic subgrid scale modeling in large eddy simulation, Phys. Fluids 14 (2002) 3616–3623.
[18] N. Park, K. Mahesh, Reduction of the Germano-identity error in the dynamic Smagorinsky model, Phys. Fluids 21 (2009) 065106.
[19] Y. Sun, H. Qi, G. Zhang, Y. Wu, A novel dynamic subgrid-scale model based on partial-averaged velocity for large eddy simulation, Phys. Fluids 36 (2) (2024) 025114.
[20] P.S. Iyer, M.R. Malik, Efficient dynamic mixed subgrid-scale model, Phys. Rev. Fluids 9 (9) (2024) L092601.
[21] X. Hu, K. Vedula, G.I. Park, Hidden mechanism of dynamic large-eddy simulation models, Phys. Rev. Fluids 9 (7) (2024) 074607.
[22] D. You, P. Moin, A dynamic global-coefficient subgrid-scale model for large-eddy simulation of turbulent scalar transport in complex geometries, Phys. Fluids 21 (2009) 045109.
[23] J. Lee, H. Choi, N. Park, Dynamic global model for large eddy simulation of transient flow, Phys. Fluids 22 (2010) 075106.
[24] H. Suzuki, Y. Hasegawa, Dynamic subgrid-scale model constant-value estimation refined by vector-level identity in an atmospheric flow field, J. Fluid Sci. Technol. 19 (2024) JFST0035.
[25] S. Goto, J.C. Vassilicos, Energy dissipation and flux laws for unsteady turbulence, Phys. Lett. A 379 (2015) 1144–1148.
[26] W.J. Bos, R. Araki, Equilibrium and nonequilibrium statistics in inhomogeneous and unsteady turbulence, Phys. Rev. Fluids 10 (2025) 044603.
[27] M. Chitose, H. Suzuki, T. Kouchi, Attempt to compensate for effects of energy conservation error on static pressure fluctuation using sub-grid scale components with the Reynolds number dependence of isotropic/anisotropic steady turbulence, J. Phys. Conf. Ser. 2793 (2024) 012004.
[28] A. Ono, H. Suzuki, T. Kouchi, K. Tanaka, Numerical analysis validating the standard k-epsilon model for the kinetic energy of turbulence subjected to weak but long-lasting wind tunnel blockage acceleration, J. Fluid Sci. Technol. 20 (1) (2025) JFST0004.
[29] J. Kim, P. Moin, Application of a fractional-step method to incompressible Navier-Stokes equations, J. Comput. Phys. 59 (1985) 308–323.
[30] H. Suzuki, S. Hattori, S. Mochizuki, Numerical investigation using an exact solution of the effects of non-solenoidality of the viscous terms on the incompressible flow, J. Fluid Sci. Technol. 12 (2017) JFST0001.
[31] T.S. Lundgren, Linearly forced isotropic turbulence, in: Center for Turbulence Research Annual Research Briefs 2003, 2003, pp. 461–473.
[32] C. Rosales, C. Meneveau, Linear forcing in numerical simulations of isotropic turbulence: physical space implementations and convergence properties, Phys. Fluids 17 (2005) 095106.
[33] R. Onishi, Y. Baba, K. Takahashi, Large-scale forcing with less communication in finite-difference simulations of stationary isotropic turbulence, J. Comput. Phys. 230 (2011) 4088–4099.
[34] P.L. Carroll, G. Blanquart, A proposed modification to Lundgren's physical space velocity forcing method for isotropic turbulence, Phys. Fluids 25 (2013) 105114.
[35] J. Jiménez, P. Moin, The minimal flow unit in near-wall turbulence, J. Fluid Mech. 225 (1991) 213–240.
[36] S. Berti, G. Boffetta, S. Musacchio, Mean flow and fluctuations in the three-dimensional turbulent cellular flow, Phys. Rev. Fluids 8 (5) (2023) 054601.
[37] X. Gong, H. Suzuki, T. Kouchi, Multiscaled inviscid Taylor-Green vortex flow for examining energy conservation error in incompressible flows, J. Phys. Conf. Ser. 2701 (2024) 012052.
[38] H. Suzuki, K. Nagata, Y. Sakai, T. Hayase, Y. Hasegawa, T. Ushijima, An attempt to improve accuracy of higher-order statistics and spectra in direct numerical simulation of incompressible wall turbulence by using the compact schemes for viscous terms, Int. J. Numer. Methods Fluids 73 (2013) 509–522.
[39] H. Suzuki, K. Nagata, Y. Sakai, T. Hayase, Y. Hasegawa, T. Ushijima, Direct numerical simulation of fractal-generated turbulence, Fluid Dyn. Res. 45 (2013) 061409.
[40] Y. Morinishi, T.S. Lund, O.V. Vasilyev, P. Moin, Fully conservative higher order finite difference schemes for incompressible flow, J. Comput. Phys. 143 (1998) 90–124.